3. Geophysical Fluid Dynamics

Experimental study on the three dimensional spherical convections with the parameters of planetary atmospheres

Contact Person Yoshi-Yuki Hayashi
Graduate School of Mathematical Science
University of Tokyo

Research Organization Yoshi-Yuki Hayashi
Shin-ichi Takehiro[1]
Masaki Ishiwatari[2], Masahiro Hosaka[3]
Geophysical Fluid Dynamics Group,
Graduate School of Mathematical Science, University of Tokyo

Keywords spherical convection, general circulation, planetary atmospheres, angular momentum, zonal mean flow, teleconnection patterns, SST anomaly, heating response

1. Background

The grand purpose of our study is to reveal the dynamical structures which underlie the general circulations of the planetary atmospheres. It is aimed to construct a theoretical framework which is useful in describing their circulation characteristics, as tried by Golitsyn[1] since 1960's $\sim$. Our interest in due course is to recognize the atmosphere of the earth (or the climate of the earth) as one of the possible realizations in the physical parameter space observed in the solar system.

One of our procedures in revealing the possible underlying dynamics is to gather and classify atmospheric circulation patterns which might be observed under various values of planetary "external" conditions such as orbital parameters (amount and variation of the incoming solar flux), radius and rotation rate of the planet, radiation property of the atmosphere, and surface boundary setups. The sampling of the possible atmospheric circulations may be possible by numerical experiments by the use of the super computer powers.

Our search in circulation patterns is now performed for the following three major targets:

1. to reveal the possible circulations which might be realized with the earth's condition, but with strongly simplified surface and/or physical processes,
2. to reveal the possible circulations which might be realized with the values of solar flux and orbital parameters which are related to Mars, Earth and Venus,
3. to reveal the possible circulations which might be realized as convection of a spherical shell in general.

These are the targets being studied continuously from the preceding years.

The first target includes so called aqua-planet experiment, where all of the lower boundary surface is assumed to be covered by the ocean[2-4]. The aim is to answer the basic problem of the climate, that is, "where and how does it rain?". In the aqua-planet experiments performed so far, the focus has been placed on especially in searching for the idealistic precipitation distribution of the tropics. The experiment performed here is also in this category, however, the new feature is to find out the deformation of the precipitation distribution to a warm SST (sea surface temperature) anomaly placed in the tropics. The configuration is supposed to extract the effect of the warm SST region in the real Western Pacific on the general circulation patterns.

The second target is the three dimensional calculations of the so called runaway greenhouse effect. It has been argued, in relation to the evolution of the atmospheres of Venus, Earth and Mars, that there exists a limit of radiation which can be emitted from the top of the atmosphere with the ocean[5]. The interesting point is that the radiation limit predicted in the literature is not far from the value of the incoming solar flux of the present earth. It is about 300 W/m^2. The argument placed so far is presented by the use of one dimensional models. It is of interest to observe with three dimensional model to what extent the climate of present earth is stable to the variation of the solar constant. The present concern is to assess the calculation possibility of the evaporation or the freezing of the oceans.

The third target is to refine the dynamical framework of the rotating spherical convection theory, and also to acquire the description ability of the circulation patterns of the deep "atmospheres" as those of outer planets and the sun. The theory of convection in rotating spherical shells has been intensely considered by Busse and his colleagues[6]. The difficulty in their work is that the description utilized is too much mathematical, and hence it is not easy to acquire physical insight. Especially for the distribution of the angular momentum, there has not been presented any satisfactory mechanistic description.

Our activity this year has been focused on the

[1] Present affiliation: Faculty of Science, Kyushu University

[2] Present affiliation: Graduate School of Earth Environmental Science, Hokkaido University

[3] Present affiliation: Climate Research Department, Meteorological Research Institute, Japan Meteorological Agency

parameter study of the aqua planet situation with varying solar flux. According to the one-dimensional radiative-convective equilibrium model, the equilibrium state of atmosphere-ocean system diminishes (the runaway greenhouse state) when solar constant exceeds a critical value called runaway limit. The previous studies on the runaway greenhouse state almost all use the one-dimensional radiative-convective equilibrium models. The following questions have not been studied at all : 1. whether the runaway greenhouse state occur even in three- dimensional system or not, 2. if runaway state occur, how much is the value of runaway limit 3. how different are the circulation pattern of runaway states from that of present earth. The answers of above questions in case of gray atmosphere are presented in following sections

2. Experimental design

2.1 Model

The model utilized is basically the same as that used in [3]. It is the code originally produced by Dr. Numaguti of NIES, and is the version now archived and maintained by GFD-DENNOU CLUB. The model consists of the three dimensional hydrostatic system on a sphere with very crude physical processes. The dynamical part is represented by the pseudo spectral method with the triangular truncation at wavenumber 21 (T21) and 32 vertical levels. The horizontal resolution might be crucially small but still is able to represent baroclinic instability.

The cumulus parameterizations are Kuo scheme or adjustment scheme or large scale condensation only. In this report, we will describe only the results with adjustment scheme. The vertical diffusion is represented by Yamada-Meller Level II scheme. The surface fluxes are evaluated by the usual bulk formula.

The surface is all covered by the ocean (aqua-planet). The value of SST is determined by the surface heat budget. The surface has no heat capacity, i.e., so called swamp ocean.

The radiation processes utilized is the exactly the same one as that of [5]. There is no scattering. Only the water vapor absorption of long wave radiation is included. Moreover, the absorption coefficient is constant (gray atmosphere). The sun is assumed to be at the equinox position. Hence the zonal mean incoming solar flux is symmetric around the equator.

In order to enable the longer term integration of the runaway greenhouse state, we have to introduce Rayleigh damping and Newtonian cooling in the upper 7 layers, and moreover we have to introduce a vertical smoothing filter similar as [8] in temperature and horizontal wind fields.

2.2 Experimental Design

The first study performed this year is the the long term integration of the runaway greenhouse state. The long term integratons of runaway greenhouse states is impossible without introducing the damping layers and vertical filter as described in 2.1. In section 3.1, the results of 1000 day integration of runaway greenhouse state obtained by our model are presented.

The second study is to determine the three-dimensional runaway limit. The series of calculation for various solar flux are performed for this purpose. As the initial condition, rest and homogeneous temperature(280K) and homogeneous specific humidity (10^{-5}) state is given in all cases. The value of three-dimensional runaway limit determined by parameter studies are presented in section 3.2.

The third study in this year is to interprete the value of runaway limit presented in 3.2. In order to consider this problem, the difference of heat budget of equilibrium states are discussed in 3.3. Then, using the results, the reason why runaway limit is 400 is considered in 3.4.

3. Some of the Results

3.1 The long term integration of runaway greenhouse state.

The results of 1000 day integration of runaway greenhouse state are shown in Figs. 1 and 2. These figures show time sequence of global mean OLR and ground temperature, respectively. In this calculation, the averaged solar flux over globe S is 450 W/m^2, which is 1.3 times larger than the value of present earth. As shown in Figure 1, the outgoing radiation emitted from the top of atmosphere decreases and reaches 330 W/m^2 at 1000 day, though global mean inward flux is given 450 W/m^2. The reason is that the vapor amount in atmosphere increases and the atmosphere becomes opaque (In this case, global mean specific humidity and optical depth are 0.2 and 20, respectively). OLR is determined by the vertical structure of the temperature at $\tau = 1$ level in the opaque atmosphere. Besides, the temperature structure approaches the saturated water vapor pressure curve. Therefore, the value of OLR is determined by the saturated water vapor pressure curve. In Figure 1, the value of OLR approaches the value determined by above mechanism. The global mean temperature increases and reaches 370 K at 1000 day because the atmosphere only can emit the radiation much less than inward solar flux(Figure 2). This state corresponds the runaway greenhouse state discussed by the one-dimensional radiative-convecitve model [5]. Our calculation confirms that the runaway greenhouse state occurs even in three-dimensional system.

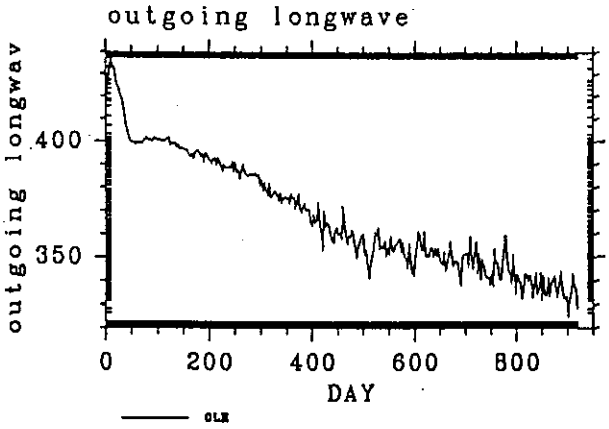

Figure 1. The time sequence of global mean OLR in runaway greenhouse state.

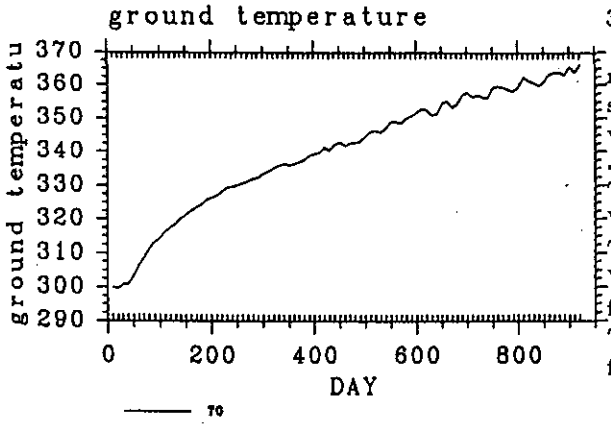

Figure 2. Same as Figure 1 except for ground temperature.

3.2 The results of parameter study

The calculations for various solar constants are performed for the purpose of determining the runaway limit of three-dimensional system. The resluts are shown in Figure 3. The relationship between the global mean OLR after 1000 day integration and the value of inward solar flux is shown in this figure. When the value of the inward flux is less than 392.5 W/m^2, the values of OLR almost equals those of inward flux and the systems reach equilibrium states. But the values of OLR become less than 350 W/m^2, in cases with solar flux larger than 400 W/m^2. In these cases, both of the ground temperature and moister content increase and the runaway greenhouse states occur as discussed in 3.1. As the result, the value of runaway limit of three-dimensional gray atmosphere is 400 W/m^2.

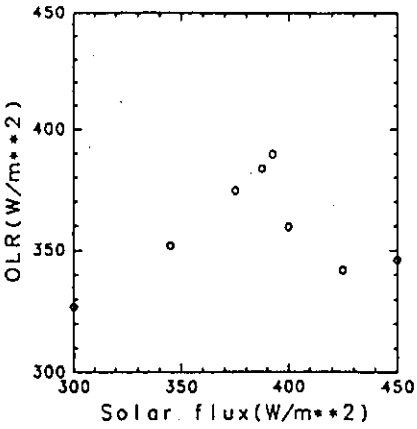

Figure 3. The relationship between the global mean inward solar flux and calculated global mean OLR.

3.3 The heat balance in the equilibrium states

In this section, we overview how the equilibrium state changes increasing solar fluxes. Figure 4 shows the zonally averaged OLR for equilibrium states, which are case of S = 300 W/m^2, S = 345 W/m^2, S = 375 W/m^2, S = 387.5 W/m^2 and S = 392.5W/m^2. These results show that the value of tropical OLR is 400 W/m^2 when global mean solar flux exceeds 375 W/m^2. The values of OLR in higher latitude also approach 400 W/m^2 when solar flux increases. The latitudinal difference of ground temperature also decrease (Figure 5). Therefore, both of OLR and temperature distribution flatten increasing solar flux.

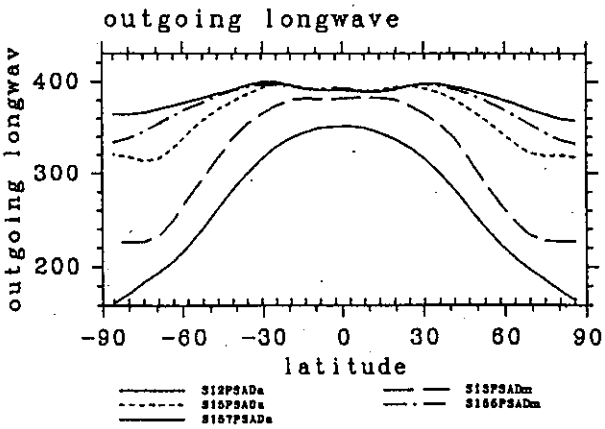

Figure 4. The latitudinal distribution of OLR for various solar fluxes. The value of solar fluxes given are 392.5 W/m^2, 387.5 W/m^2, 375 W/m^2, 345 W/m^2, 300 W/m^2.

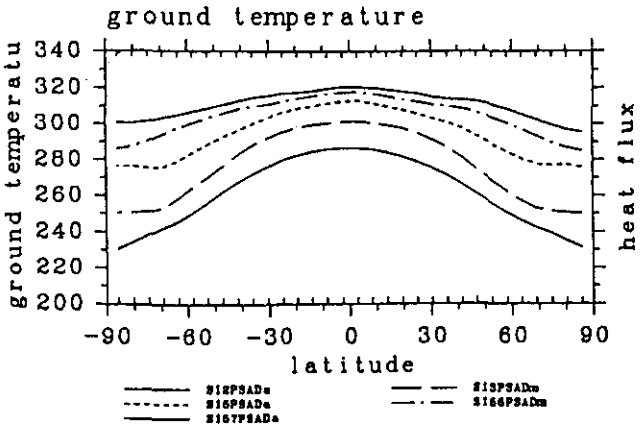

Figure 5. Same as Figure 4 except for ground temperature.

To consider the reason of flattening of OLR and ground temperature distributions, we compare the energy flux distribution of the case of $S = 345$ W/m^2 which is the value corresponding to the present earth condition, and the case of $S = 392.5$ W/m^2 which is the value slightly less than runaway limit(Figures 6 and 7). Firstly, ground fluxes are considered. When solar flux increase, the atmosphere becomes opaque and net radiation flux at the surface decrease. Then, evaporation flux increases because of surface energy balance. Especially in tropics, the evaporation flux dominates. Because the evaporation process has negative feedback effect for ground temperature changes, the temperature change in tropics is less than that in higher latitude as shown in Figure 5. Next, the heat source of atmosphere is considered. The condensation heating dominates in tropics and 60 degrees. The increased condensation at 60 degrees warms the higher latitude atmosphere. Therefore latitudinal differences of OLR and ground temperature decrease increasing solar flux.

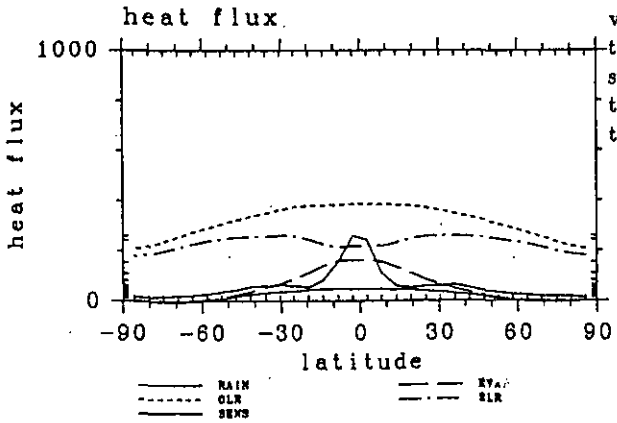

Figure 6. The latitudinal distribution of energy fluxes for the case of $S = 345$ W/m^2. RAIN, EVAP, OLR, SLR, sens are the condensation heating, evaporation flux, radiation flux emitted from the top of atmosphere, net radiation flux at the ground, sensible heat flux, respectively.

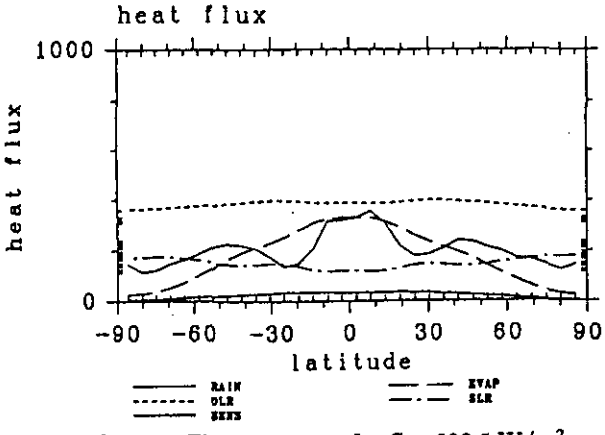

Figure 7. Same as Figure 6 except for $S = 392.5$ W/m^2.

3.4 The interpretation of runaway limit of three-dimensional system

As shown in 3.3, the value of OLR approaches 400 W/m^2 in all latitudes. Therefore, whether the runaway greenhouse state occur or not depends only the global mean value of inward solar flux. In this section, we consider the reason why the asymptotic value of OLR is 400 W/m^2. Figure 8 shows the contributions of each level to the OLR for the case of $S = 392.5$ W/m^2. Figure 8 implies that the temperature structure at the level of $\sigma \sim 10^{-0.5}$ is most important for the OLR. The temperature structure at the level almost equals the adiabatic profile(Figure 9). These figures suggest that the asymptotic value of OLR at the equator can be described by the radiative-convective equilibrium model. We also consider the effect of relative humidity, because the tropospheres obtained by three-dimensional calculations are not saturated. The typical value of relative humidity in the tropics is about 65 % for the case of $S = 392.5$ W/m^2(Figure 10). The upper limit of OLR of equilibrium solution with this value of relative humidity is 390 W/m^2 and equals the three-dimensional runaway limit(Figure 11). As the results, three-dimensional runaway limit is determined by the condition that equilibrium solution, in which relative humidity is taken into account, can exist.

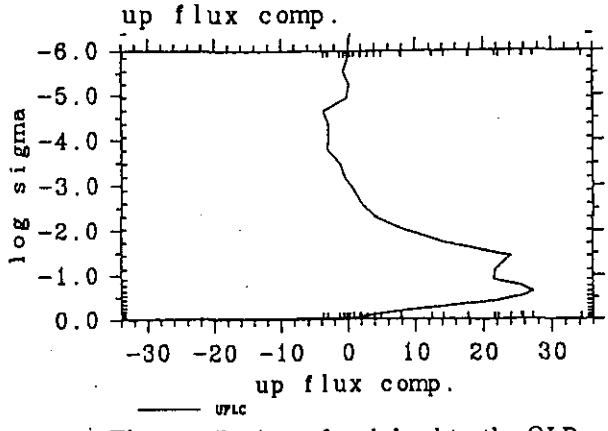

Figure 8. The contributions of each level to the OLR for the case of $S = 392.5$ W/m^2.

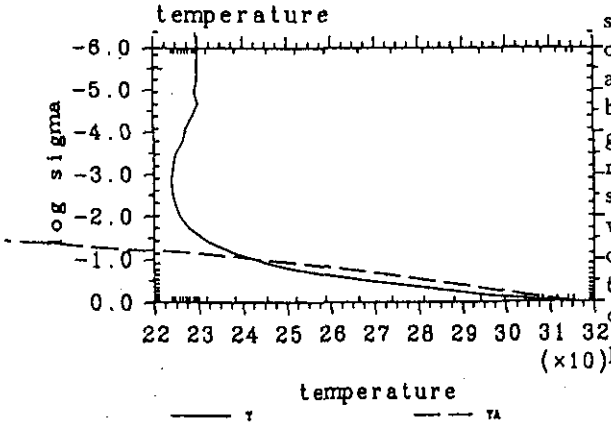

Figure 9. The temperature structure for the case of $S = 392.5$ W/m^2 (thick line) and the adiabatic temperature (dashed line).

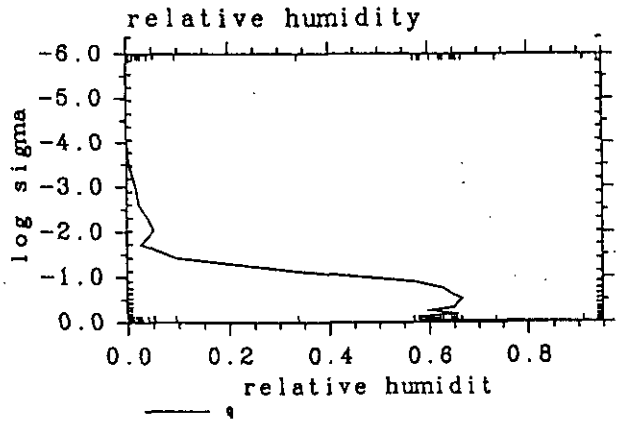

Figure 10. The vertical structure of relative humidity at the equator for the case of $S = 392.5$ W/m^2.

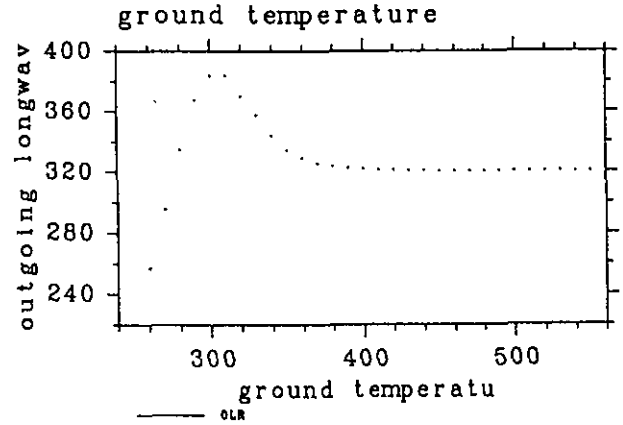

Figure 11. OLR of one-dimensional equilibrium atmosphere with 65 relative humidity.

Acknowledgment

We wish to thank Drs. Mitsumoto, Numaguti, Sugata, Takayabu and other NIES staff members for providing us with this powerful computing facility. A number of suggestions and supports by Dr. Numaguti and Sugata on softwares, hardware usages, and sciences were indispensable to our research performance. Our software environment was provided from the resources of GFD DENNOU CLUB. GFD DENNOU CLUB is an independent group of scientists aiming at collecting basic software resources for research and education of geophysical fluid dynamics and related fields. Those resources include three dimensional spherical primitive system originally developed by Dr. Numaguti while he was at University of Tokyo. We also have to express our thanks to the staffs of TISN (Tokyo university International Science Network) in providing us with data connection between NIES and University of Tokyo.

References

1. G.S. Golitsyn, *ICARUS*, 13, 1 (1970)
2. Y.-Y. Hayashi and A. Sumi, *J. Met. Soc. Japan*, 64, 451 (1986)
3. A. Numaguti and Y.-Y. Hayashi, *J. Met. Soc. Japan*, 69, 541 (1991)
4. A. Numaguti, *J. Atmos. Sci.*, 50, 1874 (1993)
5. S. Nakajima, Y.-Y. Hayashi and Y. Abe, *J. Atmos. Sci.*, 49, 2256 (1992)
6. K.-K. Zhang and F.H. Busse, *Geophys. Astrophys. Fluid Dynamics.*, 39, 119 (1987)
7. E. Manzini and K. Hamilton, *J. Atmos. Sci.*, 50, 2180 (1993)
8. R. Shaprio, 1971: *J. Atmos. Sci.*, 28, 523.

Three-Dimensional Numerical Simulation of Fluid Forces Acting on a Spinning Sphere in a Linear Shear Flow

Contact Person — Professor, Satoru Komori
Dept. of Chemical Engineering, Kyushu University

(Research Organization) — PhD Student, Ryoichi Kurose
Dept. of Chemical Engineering, Kyushu University

Research Associate, Kouji Nagata
Dept. of Chemical Engineering, Kyushu University

Section Head, Shunji Takeshita
National Institute for Environmental Studies,
Environmental Agency of Japan

Senior Scientist, Kunio Kohata
National Institute for Environmental Studies,
Environmental Agency of Japan

Keywords — drag, lift, spinning sphere, linear shear flow, numerical simulation

1. Background

Particle motions in the turbulent boundary layer are often seen in significant environmental problems such as desertification and air pollution, and they also occur in many industrial processes. It is, therefore, of great practical interest to investigate particle motions both in settling environmental problems and in designing industrial equipment. Particle motions in turbulent flows have often been investigated using numerical simulations. However, most of the numerical simulations were limited to small nonspinning particles at low particle Reynolds numbers of $Re < 1$, since drag and lift acting on a small particle comparable to or less than Kolmogorov scale can easily be given by analytical formulas based on the Stokes's assumption. On the other hand, motions of large particles at high particle Reynolds numbers of $Re > 100$ have not been simulated, because of the difficulty for estimating the lift and drag acting on large particles.

2. Objective

The purpose of this study is to numerically investigate the effects of fluid shear and particle spin on particle lift and drag in a linear shear flow at high particle Reynolds numbers. Three-dimensional numerical solutions were obtained for a steady, linear shear flow past a spinning or non-spinning spherical particle over a wide range of particle Reynolds number ($0.5 < Re < 500$), and the effects of shear and spin rate on lift and drag coefficients were investigated [1].

3. Numerical Simulation

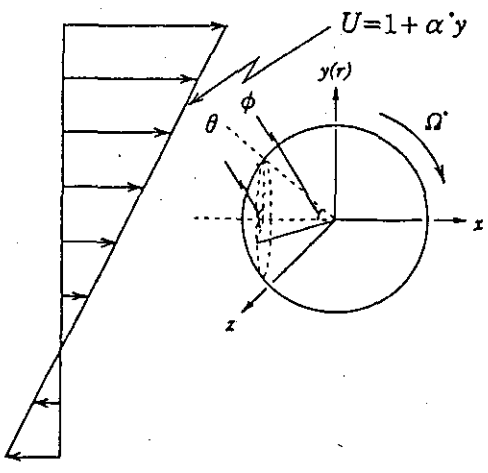

Fig.1 Coordinate system for a spinning sphere in a linear shear flow.

A three-dimensional numerical simulation was used to estimate particle lift and drag induced by

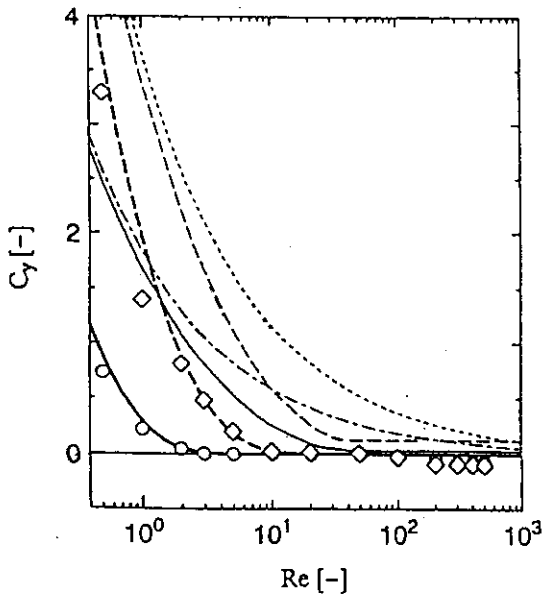

Symbol

α^*	0.1	0.4
Saffman[3]	———	- - - - -
McLaughlin[5]	———	- - - - -
Mei[4]	- - - - -	.....
Present computation	o	◇

Fig.2 Comparison of the shear lift coefficient C_y for a stationary sphere in a linear shear flow between the present and previous[3,4,5] studies ($0.5 < Re < 500$).

fluid shear and particle spin (Fig.1). The imposed flow was a linear shear flow without turbulence. The three-dimensional Navier-Stokes equations were directly solved using a third-order finite difference scheme based on the marker and cell method and the cylindrical coordinates were used[2]. Three parameters; the particle Reynolds number $Re(= 2aU_c/\nu)$, the dimensionless fluid shear rate $\alpha^*(= a/U_c(\partial U/\partial y)$ and the dimensionless particle spin rate $\Omega^*(= \Omega a/U_c)$, were defined and they ranged from 0.5 to 500, 0 to 0.4 and 0 to 0.25, respectively. Here U_c is the fluid velocity at the central point of a spherical particle, a the radius of a spherical particle and Ω the particle spin rate.

4. Results

Figure 2 shows the variations of the shear lift coefficient C_y with Re for a stationary sphere in a linear shear flow. C_y rapidly decreases with increasing Re in the low particle Reynolds number region ($Re < 10$). Although the present C_y deviates from the predictions by Saffman[3] and Mei[4], it is in good agreement with the prediction by McLaughlin[5] who extended the analytical solutions of Saffman[3] to higher Re. However, in the region of $Re > 100$, the present C_y shows the negative values in contrast with the previous results. The negative values of C_y are magnified in Fig.3. C_y becomes negative in the region of $Re > 50$, and the negative values increase with increasing α^*. In previous studies, the lift force has been considered to act towards the high speed region ($C_y > 0$). Only Jordan and Fromm[6] numerically showed the negative C_y for a cylinder with $Re = 400$ in a linear shear flow, but they did not discuss why C_y becomes negative.

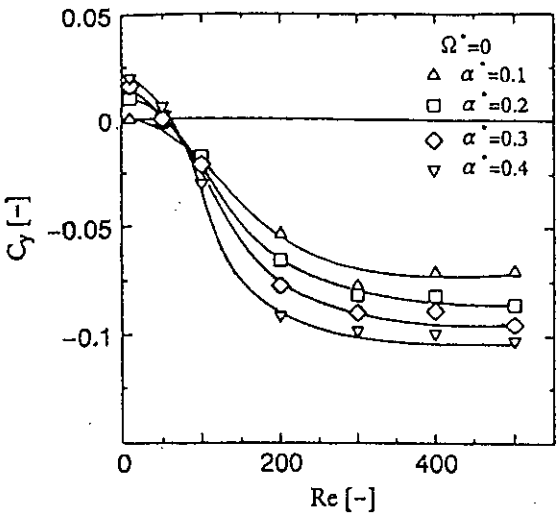

Fig.3 Shear lift coefficient C_y for a stationary sphere in a linear shear flow ($10 < Re < 500$).

To investigate the negative lift, the effects of pressure and viscous forces on C_y were estimated. The results showed that the pressure force significantly contributes to the negative C_y but the viscous force has no effect on the negative C_y. In fact, the instantaneous pressure distributions on the surface of a stationary sphere show that the pressure force acts on the rear part of the sphere in the negative y direction as indicated by an arrow B in Fig.4a for a high particle Reynolds number of $Re = 200$, in contrast with the low Reynolds n-

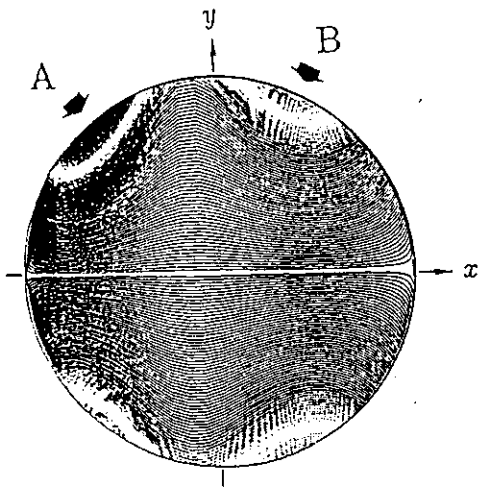

(a) for $Re = 200$ and $\alpha^* = 0.2$.

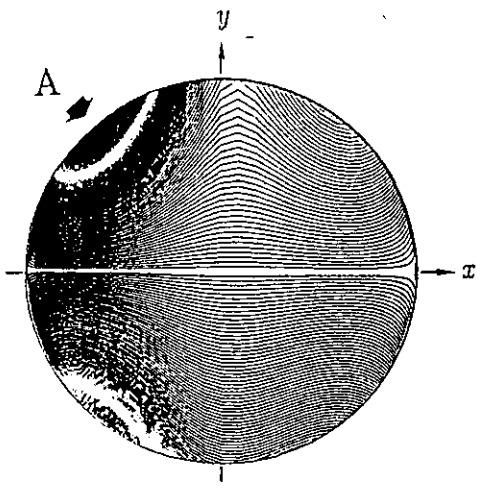

(b) for $Re = 50$ and $\alpha^* = 0.2$.

Fig.4 Surface contours of y-component of pressure on the surface of a stationary sphere.

umber case of $Re = 50$ (Fig.4b). The negative lift coefficient was also confirmed by carrying out an experiment of a falling iron-particle in a linear high-viscosity shear flow produced between two belts moving in the counter direction.

For a spinning particle, particle spin promotes the particle drag and lift as well as fluid shear. However, the sign of the lift coefficient does not change even in the high particle Reynolds number region. Figure 5 shows the distributions of the lift coefficient against the dimensionless spin rate Ω^* at $Re = 200$ for a spinning sphere in a linear shear flow. The solid lines indicate the lift coefficient $C_y^{\alpha+\Omega}$ at $Re = 200$ for a spinning particle in a linear shear flow, and the dashed lines show the sum of the lift coefficient C_y^{α} at $Re = 200$ for a stationary sphere in a linear shear flow and the lift coefficient C_y^{Ω} for a spinning sphere in a uniform unsheared flow. Although the values of $C_y^{\alpha+\Omega}$ are close to those of $C_y^{\alpha} + C_y^{\Omega}$, $C_y^{\alpha+\Omega}$ does not strictly coincide with $C_y^{\alpha} + C_y^{\Omega}$. This means

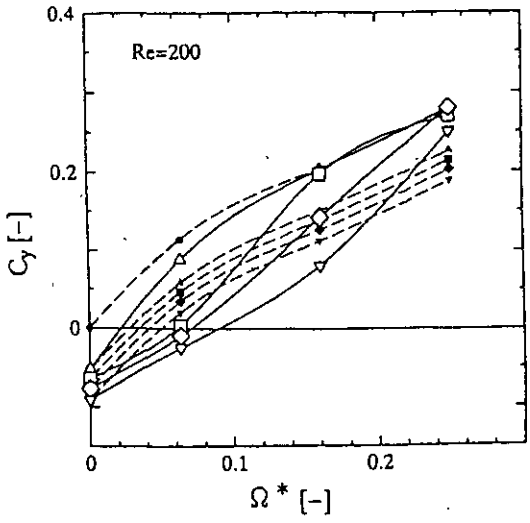

Fig.5 Lift coefficient C_y on a spinning sphere in a linear shear flow.

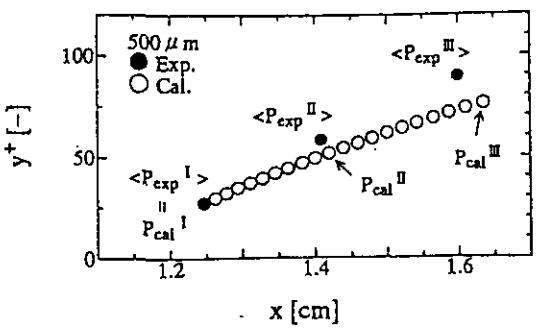

Fig.6 Comparison of the particle trajectory predicted under the mean velocity field with the trajectory measured in the turbulent boundary layer.

that the effects of fluid shear and particle spin rate cannot be independently treated for a spinning particle in a shear flow.

By using the predictions of the particle lift and drag coefficients, a trajectory of a spinning particle at high particle numbers was simulated under the mean velocity field in the turbulent boundary layer by solving a Lagrangian equation of particle motion. The predicted trajectory is compared with the measured trajectory [7] in Fig.6. The result shows that the organized motion, which cannot be given only by the mean velocity field, strongly affects the particle motion in the turbulent boundary layer.

Acknowledgements

The computation was carried out by the super computer SX-3 of Central for Grobal Environmental Research, National Institute for Environmental Studies.

References

1. Komori, S. and Kurose, R. : The effects of shear and spin on particle lift and drag in a shear flow at high Reynolds number, *Advances in Turbulence VI*, KLUWER ACADEMIC PUBLISFHERS (1996), 551-554.
2. Hanazaki, H. : A numerical study of three-dimentional stratified flow past a sphere, *J. Fluid Mech.* **192** (1988), 393-419.
3. Saffman, P.G. : The lift on a small sphere in a slow shear flow, *J. Fluid Mech.* **22** (1965), 385-400.
4. Mei, R. : An approximate expression for the shear lift force on a spherical particle at finite Reynolds number, *Int. Multiphase Flow* **18** (1992), 145-147.
5. McLaughlin, J.B. : Inertial migration of a small sphere in linear shear flows, *J. Fluid Mech.* **224** (1991), 261-274.
6. Jordan, S.K. and Fromm, J.E. : Laminar flow past a circle in a shear flow, *Phys. of Fluid* **15** (1972), 972-976.
7. Kurose, R. and Komori, S. : Relationship between particle motion and turbulence structure in turbulent boundary layer flow over particle-rough wall, *J. JSME (in Japanese)* **61** (1995), 1693-1700.

An Accurate Second-Order Approximation Factorization Method for Time-Dependent Incompressible Navier-Stokes Equation in Spherical Polar Coordinates

Contact Person *Weiming Sha*
Department of Mechanical Engineering
Nagoya Institute of Technology, Japan
Research Organization *Hiromasa Ueda*
Research Institute for Applied Mechanics
Kyushu University, Japan

Keywords Numerical Method, Incompressible Navier-Stokes Equations
Spherical Couette Flow, Spherical Polar Coordinates

1. Introduction

The numerical solution of the unsteady incompressible Navier-Stokes equations requires discretization in both space and time, and the discretized equations for the velocity and the pressure are a coupled system with the incompressibility condition. As these primitive variables are coupled and together they form a large system, it is very expensive to compute it directly. The coupling between the velocity and the pressure by the incompressibility condition is one of the main concern in designing an efficient and accurate time integration algorithm for this system.

Split step (time splitting) method may be used as an approximation approach in which the solution of an evolution equation is advanced in time by solving a set of simple problems, each of which gives a different aspect of physics. For solving the incompressible time-dependent Navier-Stokes equations, the pressure splitting algorithm, which was first introduced by Chorin [1], treats the pressure term and other terms separately and sequentially. Many authors developed the Chorin's idea, and several versions of his algorithm have be proposed since then, e.g., fractional step method (Kim and Moin [2]), pressure correction method (Van Kan [3]), projection method (Bell, Colella and Glaz [4]; Gresho [5]). Essence of the aforementioned methods is to compute an intermediate vector field in a first step by ignoring the incompressibility constraint and then projects the vector field onto a divergence-free field in a second step to obtain the velocity field. This decoupling process leads to several smaller decouple systems for velocity components and the pressure, respectively, so the computational cost of calculations of the incompressible time-dependent Navier-Stokes equations can be significantly reduced in the velocity-pressure formulation. However, the above methods have two fundamental problems, i.e., subtle boundary conditions for the intermediate velocity and the pressure, and low accuracy in time integration. Fortunately, these defects were remedied recently by Dukowicz and Dvinsky [6], and Perot [7,8]. They considered the full discretized equations in which the boundary conditions had already been applied, and therefore no ad-hoc boundary conditions of the intermediate primitive variables are required. They also analyzed the full discretized equations with an approximate factorization method (Dukowicz and Dvinsky [6]) and an approximate block LU factorization method (Perot [7]), respectively, and showed the possible second or even higher order time accuracy.

In this paper, we present a finite-difference scheme for solving the three dimensional incompressible time-dependent Navier-Stokes equations in spherical polar coordinates. Singularities of the Navier-Stokes equations in spherical polar coordinates can be removed by performing spatial discretization on a conservative form of the equations on a staggered grid. Based on Dukowicz and Dvinsky's approximate factorization method, a new algorithm, which is a second-order accurate in time and space, will be given. Then, the spherical Couette flow between two concentric rotating spheres is computed with this numerical method, and its feasibility for computing flow dynamics in spherical polar coordinates is verified. So far as we know, there is still no literature on the work. In the next, the governing equations and boundary conditions are presented in Section 2. The numerical method is described in detail in Section 3. In Section 4, we show some numerical results of the spherical Couette flow and a comparison with available numerical results and experimental measurements. A summary is given in Section 5.

2. Governing Equations and Boundary Conditions

The full incompressible Navier-Stokes equations with no body force and the continuity equation are

$$\frac{\partial \mathbf{u}}{\partial t} + \mathbf{u} \cdot \nabla \mathbf{u} = -\nabla p + \frac{1}{Re} \nabla^2 \mathbf{u} \tag{2.1}$$

$$\nabla \cdot \mathbf{u} = 0 \tag{2.2}$$

where u is the velocity field, p is kinematic pressure and Re is the Reynolds number.

We consider the time-dependent motion of an isothermal, incompressible, Newtonian fluid contained in an annulus between two concentric rotating spheres (see Figure 1). The spheres are assumed to be rigid and the cavity region between the spheres is fulled with a viscous fluid. The inner sphere is constrained to rotate about the vertical axis Z with a prescribed angular velocity Ω, while the outer sphere is fixed. The inner and outer radii of the spheres are R_1 and R_2, respectively. The Reynolds number is defined as $\mathrm{Re}=\frac{\Omega R_1^2}{\nu}$ which ν is the kinematic viscosity.

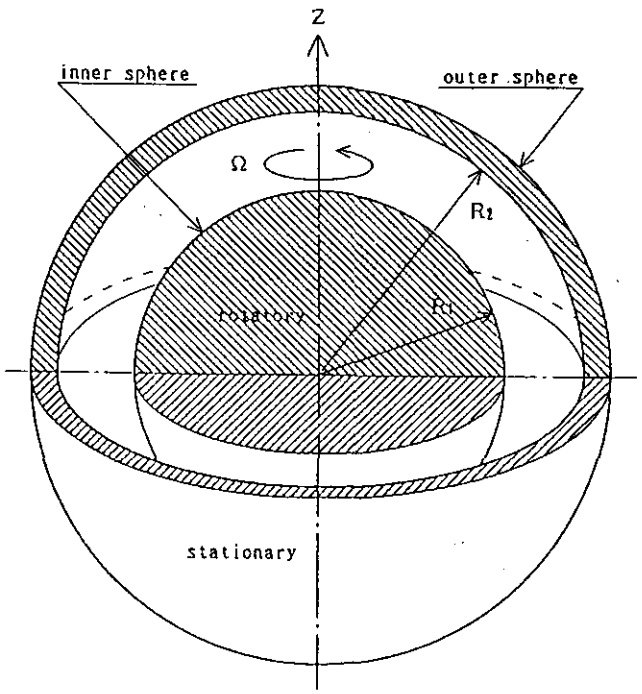

Fig. 1. Spherical Couette flow geometry

No-slip (rigid) boundary conditions along the spherical boundaries are

$$u_r=u_\theta=0,\ u_\varphi=\sin\theta \quad \text{on } r=R_1,$$

$$u_r=u_\theta=u_\varphi=0 \quad \text{on } r=R_2.$$

3. Numerical Method

3.1 Temporal and Spatial Discretization in Spherical Polar Coordinates

For brevity, we explain our discretization method with the equations (2.1), (2.2). Temporal and spatial discretization of the equations (2.1), (2.2) produces a discretized equations in the form

$$\begin{bmatrix} I-\frac{\Delta t}{2\mathrm{Re}}L & 0 \\ 0 & I \end{bmatrix}\begin{bmatrix} I & \frac{\Delta t}{2}G \\ \frac{\Delta t}{2}D & 0 \end{bmatrix}\begin{bmatrix} u^{n+1}-u^n \\ 3p^{n+1}+p^n \end{bmatrix}=$$

$$\Delta t\begin{bmatrix} \frac{1}{\mathrm{Re}}L & G \\ -\frac{1}{2}D & 0 \end{bmatrix}\begin{bmatrix} u^n \\ p^n \end{bmatrix}+\Delta t\begin{bmatrix} -\frac{1}{2}(3Hu^n-Hu^{n-1}) \\ 0 \end{bmatrix} \tag{3.2b}$$

The equation (3.2b) is exactly equivalent to the following split equations in which two new intermediate velocities included;

$$\hat{u}=u^n+\frac{\Delta t}{2}Gp^n \tag{3.2c}$$

$$\left(I-\frac{\Delta t}{2\mathrm{Re}}L\right)\tilde{u}=\left(I+\frac{\Delta t}{2\mathrm{Re}}L\right)\hat{u}-\frac{\Delta t}{2}[3Hu^n-Hu^{n-1}] \tag{3.2d}$$

$$u^{n+1}=\tilde{u}-\frac{3\Delta t}{2}Gp^{n+1} \tag{3.2e}$$

$$Du^{n+1}=0 \tag{3.2f}$$

Taking the divergence of equation (3.2e) and using the incompressibility condition equation (3.2f), we can obtain the following discrete Poisson equation for the pressure;

$$\frac{2}{3}\frac{D\tilde{u}}{\Delta t}=DGp^{n+1}=Lp^{n+1} \tag{3. 2g}$$

3.3 Method for Solving the Discrete Velocity Equation (3.2d)

The approximate factorization technique (Beam and Warming [9]; Briley and McDonald [10]; Kim and Moin [2]) is used to treat the discrete velocity equation (3.2d). we can compute the

$$\mathbf{u}^{n+1}-\mathbf{u}^{n}+\frac{\Delta t}{2}[3\mathbf{H}\mathbf{u}^{n}-\mathbf{H}\mathbf{u}^{n-1}]=-\frac{\Delta t}{2}[3\mathbf{G}p^{n+1}-\mathbf{G}p^{n}]$$

$$+\frac{\Delta t}{2\mathrm{Re}}[\mathbf{L}\mathbf{u}^{n+1}+\mathbf{L}\mathbf{u}^{n}]+\Delta t(\mathbf{mbc}) \qquad (3.1a)$$

$$\nabla\cdot\mathbf{u}^{n+1}=0+(\mathrm{dbc}) \qquad (3.1b)$$

where L is the spatial discrete Laplacian viscous term (conservative part) operator, H is the spatial discrete conventive term plus remained viscous term (non-conservative part) operator, G is the spatial discrete gradient operator and D is the spatial discrete divergence operator. Δt is the time increment and the superscript n means the nth time step. The spatial discrete operators L, H, G and D are evaluated using the central finite-difference scheme on a staggered grid and are second-order accurate in space. It is noted that the boundary conditions for the momentum equation (**mbc**) and continuity equation (dbc) have been already incorporated in the discretized equations (3.1a), (3.1b), and these boundary condition vectors (**mbc**) and (dbc) should preserve a second-order accuracy of the temporal and spatial discretization. In the present study, there are clearly the periodic, homogeneous no-slip boundary conditions for the velocity. So, the boundary condition vectors are identically zero (Perot [7]), and will not appear in the following section.

3.2 Approach to the Discretized Equations (3.1a), (3.1b) with a Second-Order Approximate Factorization Method

We can easily rewrite the discretized equations (3.1a) and (3.1b) in the next matrix format

$$\begin{bmatrix} \mathbf{I}-\frac{\Delta t}{2\mathrm{Re}}\mathbf{L} & \frac{\Delta t}{2}\mathbf{G} \\ \frac{\Delta t}{2}\mathbf{D} & 0 \end{bmatrix}\begin{bmatrix} \mathbf{u}^{n+1}-\mathbf{u}^{n} \\ 3p^{n+1}+p^{n} \end{bmatrix}=$$

$$\Delta t\begin{bmatrix} \frac{1}{\mathrm{Re}}\mathbf{L} & \mathbf{G} \\ -\frac{1}{2}\mathbf{D} & 0 \end{bmatrix}\begin{bmatrix} \mathbf{u}^{n} \\ p^{n} \end{bmatrix}+\Delta t\begin{bmatrix} -\frac{1}{2}(3\mathbf{H}\mathbf{u}^{n}-\mathbf{H}\mathbf{u}^{n-1}) \\ 0 \end{bmatrix} \qquad (3.2a)$$

In a manner similar to Dukowicz and Dvinsky [6], the equation (3.2a) can be approximately factorized as

discrete velocity of equation (3.2d) by solving three tridiagonal matrices with a standard TDMA method.

3.4 Method for Solving the Discrete Piossion Equation (3.2g)

We represent the discrete Piossion equation (3.2g) definitely on a MAC staggered grid (Harlow and Welch [11]) and compute the discrete pressure, firstly, by application of ADI method (Peaceman and Rachford [12]) and then solving the system with a standard TDMA method for the two tridiagonal matrices and with a refined TMDMA method (Temperton [13]) for the cyclic tridiagonal matrix.

3.5 Overall Numerical Computation Procedure

The overall numerical computation procedure to solve the time-dependent incompressible Navier-Stokes equations is as follows:

1. Solve the intermediate velocity from the equation (3.2c);
2. Solve the intermediate velocity from the equation (3.2d);
3. Solve the pressure p^{n+1} from the equation (3.2g) with the divergence-free velocity equation (3.2f) satisfied;
4. Solve the velocity u^{n+1} from the equation (3.2e), and then finish one time step calculation.

To complete the numerical method, adequate initial conditions of the velocity u^0 and the pressure gradient Gp^0 are required. In the present study, we chose the Stokes solution as the initial velocity condition, while for the initial pressure gradient it can be found that $Gp^0=0$ is exactly satisfied. In the following calculation, the computational domain is divided by a number of grids 22*361*91 in the radial direction, meridional direction and circumferential direction, respectively. The stability of the overall numerical method is restricted by the CFL condition. In the next Section, we present the numerical results in the case of ß=0.14 in which the clearance ratio ß is defined as $ß=(R_2-R_1)/R_1$. The Reynolds number was quasi-statically increased in order to eliminate the effect of the rotative acceleration ratio on the spherical Couette flow. Time integration was carried out until the steady state was obtained. Comparisons with the numerical solutions and the experimental results are also shown to prove the validation of the numerical method.

4. Numerical Results

Figure 2 shows the meridional streamlines in meridional plane for different Reynolds number Re. Sold contours of the streamline mean counterclockwise circulation while those showing clockwise circulation are dashed. At Re=888 (see Fig. 2a), the meridional part of the basic flow consists of one large vortex in each hemisphere. The vortices rotate in opposite directions in such way that the flow at the equator is directed from the inner sphere to the outer one. The solid streamline located exactly at the equator is the outflow boundary between the two large vortices. Clearly, the zero-vortex flow is axisymmetric reflection-symmetric about the equator. As the Reynolds number Re is increased, the basic flow develops (see Fig. 2b for Re=890), and at Re=910 the pinch phenomenon is apparent (see Fig. 2c). The pinch is characterized by a stagnation point. Although the circulation

in the closed streamlines of the zero-vortex pinch has the same sign as that in the large vortex, it is not separated from the large vortex. The flow with the pinches is still reflection-symmetric about the equator. Like the Taylor-Couette flow in differentially rotating cylinders, the spherical Couette flow in some configurations of two concentric spheres with the inner one rotating, has a critical Reynolds number Re_c. That is, as the Reynolds becomes larger, such that for $Re \geq Re_c$ the first instability occurs. This first instability induces a transition to the basic flow and Taylor-Görtler vortices are then formed in the equatorial region. Figure 2d shows clearly that in each hemisphere there is one Taylor-Görtler vortex near the equator. The critical Reynolds number of this one-vortex flow is determined as Re_c=920. It can be seen that the Taylor-Görtler vortex is separated from the large basic vortex by a nearly straight streamline which is extended from the inner to the outer radial boundary. This streamline is an outflow boundary while at the equator there is an inflow boundary. The circulations in the Taylor-Görtler and the large basic vortex have the opposite sign. A comparison of our computed solution with the previous numerical work (Marcus and Tuckerman [14], Dumas and Leonard [15]) shows a very close similarity. As the Reynolds number Re is increased further, the vortex flow becomes unstable due to the secondary instability. This secondary instability results in transition to the Taylor-Görtler vortices with spiral vortices. The spiral Taylor-Görtler vortex flow is illustrated in Figure 3. It can be seen that two spirals are formed in each hemisphere. Qualitatively, the three-dimensional spiral Taylor-Görtler vortex flow, produced with the numerical method, is in very good agreement with the previous experimental results (Nakabayashi [16] and Nakabayashi and Tsuchida [17]).

6. *Summary*

A finite-difference method for solving three-dimensional, time-dependent incompressible Navier-Stokes equations in spherical polar coordinates is presented. A new algorithm, which is a second-order accurate in time and space, is considered, and decoupling between the velocity and the pressure is achieved by this algorithm. Boundary conditions of the intermediate velocities are not required as we deal with the fully discretized equation in the interior of computational domain. A staggered grid system is used in present study, so the treatment of singularities of the equations in spherical polar coordinates is simplified and the boundary condition of the discrete pressure is unnecessary. The discrete velocity equations are solved with the approximate factorization technique and standard TDMA method, while the discrete Piossion equation is solved with the ADI technique and a refined TDMA method. Further, the numerical method is tested by computing the spherical Couette flow between two concentric spheres with the inner one rotating. A comparison of the numerical solutions with available numerical results and experimental measurements was made. It is demonstrated that the initial-boundary numerical code is valid for solving three-dimensional, unsteady incompressible Navier-Stokes

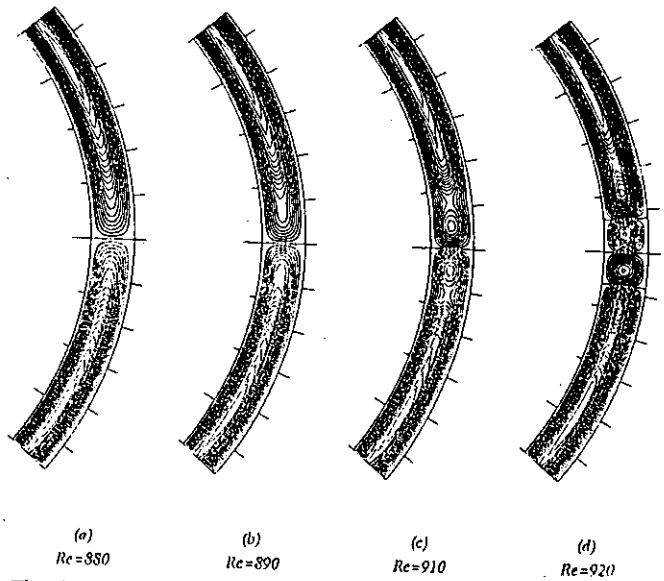

Fig. 2. Contours of the meridional streamlines for (a) Re=880; (b) Re=890; (c) Re=910; (d) Re=920.

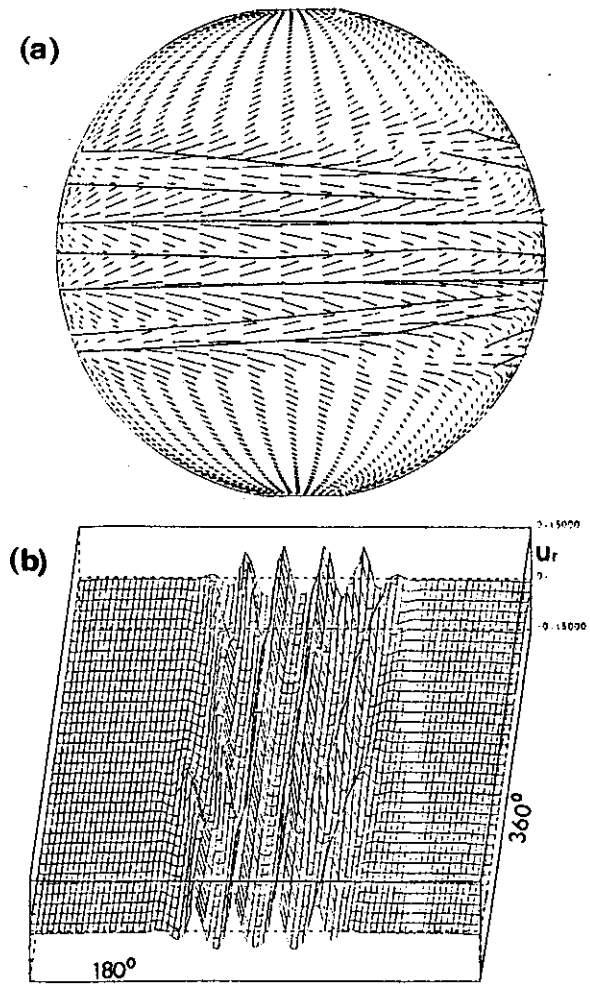

Fig. 3. Spiral Taylor-Görtler vortex flow (a) vectors ; (b) velocity u_r in the Plane.

equations in spherical polar coordinates.

Acknowledgments

This computation were carried at the computing center of National Institute for Environmental Studies, Japan.

Reference

1. A. J. Chorin, Math. Comput. 22, 745(1968).
2. J. Kim and P. Moin, J. Comput. Phys. 59, 308(1985).
3. J. Van Kan, SIAM J. Sci. Statist. Comput. 7, 870(1986).
4. J. B. Bell, P. Colella and H. M. Glaz, J. Comput. Phys. 85, 257(1989).
5. P. M. Gresho, Int. J. Numer. Methods Fluids 11, 587(1990).
6. J. K. Dukowicz and A. S. Dvinsky, J. Comput. Phys. 102, 336(1992).
7. J. B. Perot, J. Comput. Phys. 108, 51(1993).
8. J. B. Perot, J. Comput. Phys. 121, 190(1995).
9. R. M. Beam and R. F. Warming, J. Comput. Phys. 22, 87(1976).
10. W. R. Briley and H. McDonald, J. Comput. Phys. 24, 372(1977).
11. F. H. Harlow and J. E. Welch, Phys. Fluids 8, 2182(1965).
12. D. W. Peaceman and H. H. Rachford, J. Soc. Indust. Appl. Math. 3, 28(1955).
13. C. J. Temperton, J. Comput. Phys. 19, 317(1975).
14. P.S. Marcus and L.S. Tuckerman, J. Fluid Mech. 185, 1(1987).
15. G. Dumas and A. Leonard, J. Comput. Phys. 111, 205(1994).
16. K. Nakabayashi, J. Fluid Mech. 132, 209(1983).
17. K. Nakabayashi and Y. Tsuchida, J. Fluid Mech. 194, 101(1988).